



NiO nanoflakes decorated needle-like MnCo₂O₄ hierarchical structure on nickel foam as an additive-free and high performance supercapacitor electrode

Mi He¹, Linli Cao¹, Weilong Li^{1,*} , Xinwei Chang¹, Xinliang Zheng², and Zhaoyu Ren^{1,*}

¹Institute of Photonics and Photon-Technology, Northwest University, Xi'an 710069, China

²School of Physics, Northwest University, Xi'an 710069, China

Received: 22 October 2020

Accepted: 13 January 2021

Published online:
29 January 2021

© The Author(s), under exclusive licence to Springer Science+Business Media, LLC part of Springer Nature 2021

ABSTRACT

Although many researches have been made in the construction and fabrication of electrode materials for supercapacitors, it remains a difficult task to realize the application of the supercapacitor with high energy density. The binary MnCo₂O₄@NiO hierarchical electrode has been successfully fabricated on nickel foam (NF) without any binder or additives by simple hydrothermal methods and corresponding annealing processes. By virtue of constructing hierarchical core-shell structure with different morphologies and forming additive-free electrode, the composite electrode not only possesses abundant surface active sites for electrochemical reaction as well as large buffering space for volume deformation in the charging-discharging processes, but also shows the improved contacting area and electric conductivity between active substance and metal collector. The synthetic MnCo₂O₄@NiO/NF electrode presented higher specific capacitance (1186 F g⁻¹ under 1 A g⁻¹) and long cycle lifespan (maintain 91% of the original capacitance over 5000 cycles) under a high current density of 10 A g⁻¹. Further, the asymmetric supercapacitor with MnCo₂O₄@NiO/NF electrode shows higher energy density of 42.2 Wh kg⁻¹ under a power density of 748.2 W kg⁻¹. These results demonstrate that the binary MnCo₂O₄@NiO hierarchical structure is the hopeful candidate material for high performance supercapacitor electrode.

Handling Editor: Joshua Tong.

Address correspondence to E-mail: lwl@nwu.edu.cn; rzy@nwu.edu.cn

<https://doi.org/10.1007/s10853-021-05810-8>

Introduction

With rapidly developing new forms of clean power such as wind power, tidal power and solar power, energy storage and utilization put forward higher requirements to energy storage devices. Supercapacitor as a novel energy storage device has drawn increasing attention on intelligent power distribution system, transportation and miniaturized electronic devices due to excellent performance such as faster charging and discharging, long cycle lifespan, broad operating temperature range, environment friendly [1–4]. However, the ordinary energy density of supercapacitors limits further application [5]. For higher energy density, two strategies were proposed to improve energy storage performance according to the energy storage formula [6]. On one hand, employing organic electrolyte with wide voltage range and assembling asymmetric supercapacitors (ASC) can improve the potential window and thus enhance the energy density. Nevertheless, low ionic conductivity and high cost, especially chemical safety, limit the development of organic electrolyte [7]. On the other hand, making use of active materials with high specific capacity is a more direct and efficient way to promote the energy density. Therefore, designing and constructing high specific capacitance electrode materials and assembling ASCs are safe and efficient ways to enhance the energy density of supercapacitor.

Among various potential electrode materials, metal oxide has been extensively studied because of higher specific capacitance than carbon materials and more stable structure than polymer materials [2]. However, the poor conductivity of the mono-metallic oxide prevents the charge from being transferred rapidly in the electrochemical reaction and limits its electrochemical performance [8]. Therefore, a general method is to combine mono-metallic oxides with graphene, carbon nanotubes, reduced graphene oxide and other materials with better conductivity [9]. In addition, bimetallic oxides formed by new metal elements introduced into mono-metallic oxides can not only enhance electrical conductivity but also supply more redox reaction activity [10]. Typically, Co element is introduced into Mn_3O_4 to form $Mn_{2.6}Co_{0.4}O_4$, the specific capacitance of bimetallic oxides is increased from 250 to 400 mAh g^{-1} compared with mono-metallic oxides [11]. The increase is

attributable to that the presence of mixed valence of Co and Mn enhances the conductivity of Mn_3O_4 and promotes the electrochemical reaction. In recent studies, polymetallic oxides have become the potential supercapacitor materials due to the higher conductivity than mono-metallic oxides. The binary or ternary metal oxides get an increasing number of researches such as $MnCo_2O_4$ [12], $ZnCo_2O_4$ [13], $CoMn_2O_4$ [14], $ZnMn_2O_4$ [15], $ZnFe_2O_4$ [16], $NiCo_2O_4$ [17], $CoMoO_4$ [18], Mn-Ni-Co ternary oxide [19], etc.

In particular, $MnCo_2O_4$ demonstrates excellent electrochemical behavior, because Co possesses high oxidation potential, and Mn assumes more oxidation states. $MnCo_2O_4$ is considered as the potential electroactive material because of environmentally friendly, low cost, high theoretical specific capacitance [20, 21]. In addition, $MnCo_2O_4$ presents a larger lattice parameter compared with other binary metal oxides, which demonstrates a faster charge-transfer process in the electrode material interface due to the enhanced ion diffusion coefficient [22, 23]. Nonetheless, the lower specific capacitance and inferior structure stability of $MnCo_2O_4$ hinder its development as high performance electrode material [24]. A reasonable way is to design the hybrid nanostructure composite materials by combining $MnCo_2O_4$ with other electroactive materials of high theoretical specific capacitance. NiO is a potential reinforcement material because of its excellent pseudocapacitance behavior, high theoretical specific capacitance, stable structure and low cost [25]. The NiO- $MnCo_2O_4$ porous microspheres fabricated with the one-pot spray demonstrate better electrochemical performance for lithium ion batteries [26]. Further, $MnCo_2O_4@NiO$ porous nanosheet electrodes have been produced with poly(vinylidene fluoride) (PVDF) binder and acetylene black conductor, which demonstrate a specific capacitance of 508.3 F g^{-1} under 2 A g^{-1} and have capacitance retention ratio of 67.7% with the current density improved from 0.5 A g^{-1} to 6 A g^{-1} [27]. In spite of realizing some enhanced electrochemical performances of NiO- $MnCo_2O_4$ complexes, the agglomeration of electroactive material due to the randomly stacking and irregular distribution is prone to decrease the contacting surface area for conducting electrochemical reaction, which greatly limits efficient utilization of electroactive materials [28]. Besides, NiO grows on $MnCo_2O_4$ in a similar morphological structure (two mixed nanoparticles), which may result in low

surface area. Thus, this structure greatly weakens the electrochemical performance of MnCo_2O_4 and NiO composites [29]. Furthermore, the poor combination and low conductivity between electroactive substance and current collector are caused by using PVDF binder, which is a great obstacle to give full play to the performance of active materials [30]. Therefore, designing a composite electrode with better matching structure and no any binder or additives can effectively solve these problems and further enhance the electrochemical properties of electrode materials.

In our work, we successfully prepared NiO nanoflakes decorated needle-like MnCo_2O_4 hierarchical structure directly deposited on nickel foam (NF) as an additive-free and high performance supercapacitor electrode. The fabrication process of $\text{MnCo}_2\text{O}_4@$ -NiO/NF electrode is briefly illustrated in Fig. 1. On one hand, one-dimensional needle-like MnCo_2O_4 not only ensures high conductivity and specific capacitance but also provides sufficient sites for NiO growth on the whole side. On the other hand, NiO flakes grow in a different morphological structure from MnCo_2O_4 to form the hierarchical structure, which provides abundant surface active sites for Faraday reaction as well as large buffering space for volume deformation in the charging-discharging processes. What's more, in situ synthesis without additives not only increases the contacting area and electric conductivity between electroactive substance and metal collector, but also supplies plenty of room for transporting electrolyte ions. Then, the electrochemical performance of the MnCo_2O_4 /NF, NiO/NF and $\text{MnCo}_2\text{O}_4@$ NiO/NF was compared by using 2 M KOH as the electrolyte. Through electrochemical impedance spectrum and diffusion coefficient analysis, the performance of composite electrode is further understood. Finally, the performance of the composite electrode in practical device is evaluated by assembling ASCs. The results present that the

$\text{MnCo}_2\text{O}_4@$ NiO/NF electrode is a hopeful electrode material for supercapacitor.

Experimental

Preparation of MnCo_2O_4 /NF electrode

In a typical synthetic process of needle-like MnCo_2O_4 electrode: firstly, NF ($1 \times 2 \text{ cm}^2$) was washed with ultrasound in acetone, ethanol and ultrapure water, respectively, and then dried in a vacuum stove. Secondly, 0.8 mmol $\text{Mn}(\text{NO}_3)_2 \cdot 4\text{H}_2\text{O}$, 1.6 mmol $\text{Co}(\text{NO}_3)_2 \cdot 6\text{H}_2\text{O}$, 4 mmol urea and 1.6 mmol NH_4F were added into 40 ml ultrapure water and then vibrated magnetically for an hour to derive the uniform pink solution. Thirdly, transferring the solution and the clean NF into a 50 mL reactor, which was placed in the oven for a complete reaction of 7 h at $140 \text{ }^\circ\text{C}$, and then naturally cooled to ambient temperature. After reaction, the samples were cleaned with ultrapure water about 5 times and subsequently dried in the oven at $60 \text{ }^\circ\text{C}$ for 12 h. Finally, dried sample was put in a tubular furnace, temperature of tubular furnace was increased from $22 \text{ }^\circ\text{C}$ to $400 \text{ }^\circ\text{C}$ in 200 min, keeping $400 \text{ }^\circ\text{C}$ for 3 h in air atmosphere, then down to room temperature naturally.

Preparation of $\text{MnCo}_2\text{O}_4@$ NiO/NF electrode

$\text{MnCo}_2\text{O}_4@$ NiO hierarchical structure was further prepared through the approach similar to the MnCo_2O_4 . First, 0.291 g $\text{Ni}(\text{NO}_3)_2 \cdot 6\text{H}_2\text{O}$ and 0.601 g urea were dissolved in 40 ml ultrapure water and then vibrated for half an hour to derive the light green solution. Next, the solution and MnCo_2O_4 /NF were put to 50 mL reactor, which was placed in the oven for 8 h at $100 \text{ }^\circ\text{C}$. The sample loaded on NF and the powder precipitation at the bottom of the reactor were cleaned with ultrapure water about 5 times, and subsequently dried in the oven under $60 \text{ }^\circ\text{C}$ for 12 h.

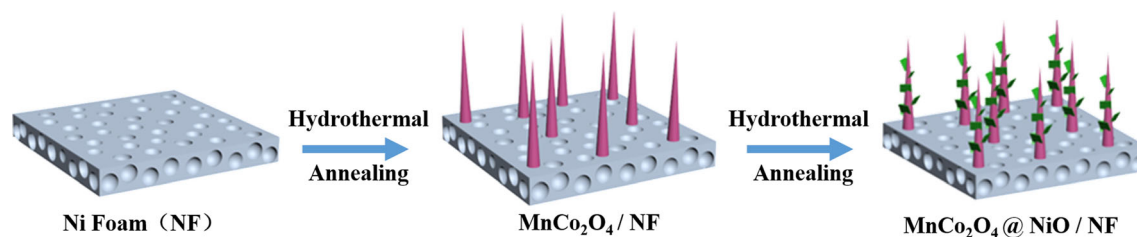


Figure 1 Schematic illustrating the fabrication process of the $\text{MnCo}_2\text{O}_4@$ NiO/NF electrode.

Finally, these samples were placed in the tube furnace, and temperature of tubular furnace was increased from 22 °C to 300 °C in 200 min, keeping 300 °C and anneal 3 h under air atmosphere, then down to room temperature naturally. The mass loading of the $\text{MnCo}_2\text{O}_4@\text{NiO}$ composites on the NF is about 0.6 mg cm^{-2} .

Characterization of prepared samples

The composition and structure of materials were detected with powder X-ray diffraction (XRD, Bruker D8 ADVANCE). The surface chemical state of materials was studied with X-ray photoelectron spectrometer (XPS, VG ESCA Lab220I-XL). Morphologies of materials were distinguished by scanning electron microscope (SEM, Carl Zeiss SIGMA) and transmission electron microscope (TEM, FEI Tecnai G2 F20).

Electrochemical measurements

All electrochemical tests of the synthesized materials were conducted on electrochemical workstations (CHI 660D, Chenhua, Shanghai). The electrochemical properties of the materials were researched via three-electrode setup which consists of as-fabricated electrode as the work electrode, Pt plate as the counter electrode, the Hg/HgO as the reference electrode and 2 M KOH as the electrolyte.

The performance of ASC device was tested by two-electrode system which is made up of positive electrode of $\text{MnCo}_2\text{O}_4@\text{NiO}/\text{NF}$, negative electrode of activated carbon (AC) and 2 M KOH as the electrolyte. Due to easy comparison with the results of other researches, AC as the usual negative electrode material was selected for the ASC device. Based on the formula of charge balance theory (details in Supporting Information), the active mass loading of the AC electrode in ASC device could be computed by the voltage range and specific capacitance of the two-electrodes as well as the active mass of positive electrode. Therefore, the active mass loading of the AC electrode in the ASC device is around 3.6 mg cm^{-2} . The AC-based electrode was compounded by the following steps: (1) blending the AC, acetylene black and polytetrafluoroethylene in a weight ratio of 8:1:1 in ethanol; (2) Coating the well-mixed paste to NF substrate; (3) The coated electrode was then dried under 80 °C for 6 h.

Results and discussion

For the sake of determining the structure and composition of the prepared materials, the XRD test of samples was executed. Figure 2 is the XRD curves of three different electrode materials produced during the experiment. The red, black and blue curves are the MnCo_2O_4 powder of the first step hydrothermal reaction, the NiO powder of the second step hydrothermal reaction and the $\text{MnCo}_2\text{O}_4@\text{NiO}/\text{NF}$ electrode. For the red curve, diffraction peaks appear in 18.5° , 30.5° , 36° , 37.6° , 43.8° , 54.3° , 57.9° and 66.8° , which is consistent with (1 1 1), (2 2 0), (3 1 1), (2 2 2), (4 0 0), (4 2 2), (5 1 1) and (5 3 1) crystal faces of the MnCo_2O_4 (JCPDS card no. 23–1237). Further, there are no other peaks in the red curve, which proves that the prepared sample is of high purity. Diffraction peaks of the black curve appear in 37.2° , 43.3° , 62.85° , 62.9° , 75.4° and 79.4° , which corresponds to (1 0 1), (0 1 2), (1 1 0), (1 0 4), (1 1 3) and (2 0 2) crystal faces of the NiO (JCPDS card no. 44-1159). The clear peak shape implies that the purity of the fabricated material is relatively high. The XRD result of the $\text{MnCo}_2\text{O}_4@\text{NiO}/\text{NF}$ is presented in the blue curve. It can be seen in the curve that the strength of three peaks at 44.5° , 51.8° and 76.4° is far higher than that of other peaks, which is related to (1 1 1), (2 0 0) and (2 2 0) crystal faces of the Ni (JCPDS card no. 04-0850) in NF. Besides, there are only peaks from the MnCo_2O_4 and NiO without peaks of impurities and other phases. Therefore, the structure and composition of the $\text{MnCo}_2\text{O}_4@\text{NiO}/\text{NF}$ sample were well confirmed.

In addition to XRD, the XPS is conducted to further understand the chemical state of the sample elements. A wide range of XPS was measured from 0 to

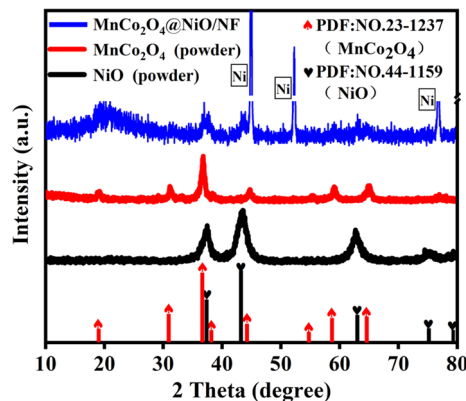


Figure 2 XRD patterns of the MnCo_2O_4 , NiO powder and $\text{MnCo}_2\text{O}_4@\text{NiO}/\text{NF}$.

1100 eV, and the result was shown in Fig. 3a. In this figure, the peaks of the five identifiers represent the elements that appear during testing. Among them, C 1 s peak comes from the test environment such as air pollution. The O 1 s, Mn 2p, Co 2p and Ni 2p peaks are derived from the sample. In the Fig. 3b, the peaks at 855.0 eV and 872.1 eV are, respectively, originated from Ni 2p_{3/2} and Ni 2p_{1/2}, and the peaks at 861.5 eV, and 880.0 eV are satellite peaks [31]. Further, both Ni 2p_{3/2} and Ni 2p_{1/2} were divided into two chemical states, which presents the coexistence of chemical states of Ni²⁺ and Ni³⁺ in materials [32]. Figure 3c shows four peaks associated with Co element. In particular, 780.4 eV and 795.7 eV are in accordance with Co 2p_{3/2} and Co 2p_{1/2} spin orbital peaks, respectively [33]. These two peaks can be fitted with four weak peaks, including 779.8 eV, 780.9 eV, 795.3 eV and 796.6 eV, which imply the presence of valence state of Co³⁺ and Co²⁺ [34]. The Mn 2p_{3/2}

and Mn 2p_{1/2} peaks were observed at 642.5 eV and 653.9 eV in Fig. 3d, respectively. The splitting of each peak declares the Mn element exists in divalent and trivalent state [35]. All of these XPS spectra further confirm that the MnCo₂O₄ and NiO are present in materials.

For clearly observing the morphology of samples, SEM measurements of prepared samples were conducted, and the results were displayed in Fig. 4. According to Fig. 4a, needle-like MnCo₂O₄ was successfully grown on the NF substrate, and the appearance is dense and uniform. Through SEM diagram of high magnification in Fig. 4b, it could be found that interlaced needle-like MnCo₂O₄ grows on the substrate and the diameter of the needle-like MnCo₂O₄ is about 200 nm. For the powder deposited at the bottom of the reactor, MnCo₂O₄ agglomerates into a spherical with a diameter of about 10 μm due to the absence of basal support during the first

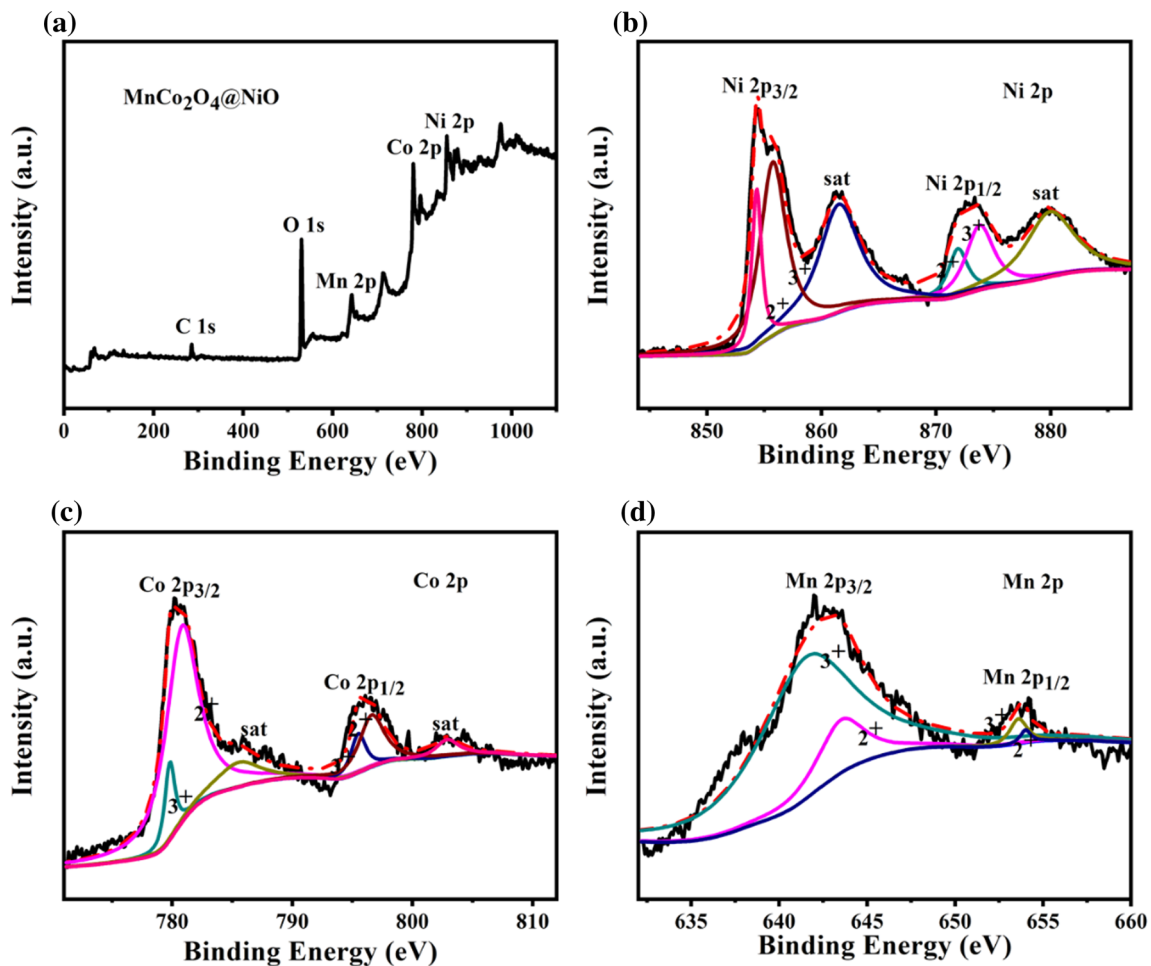
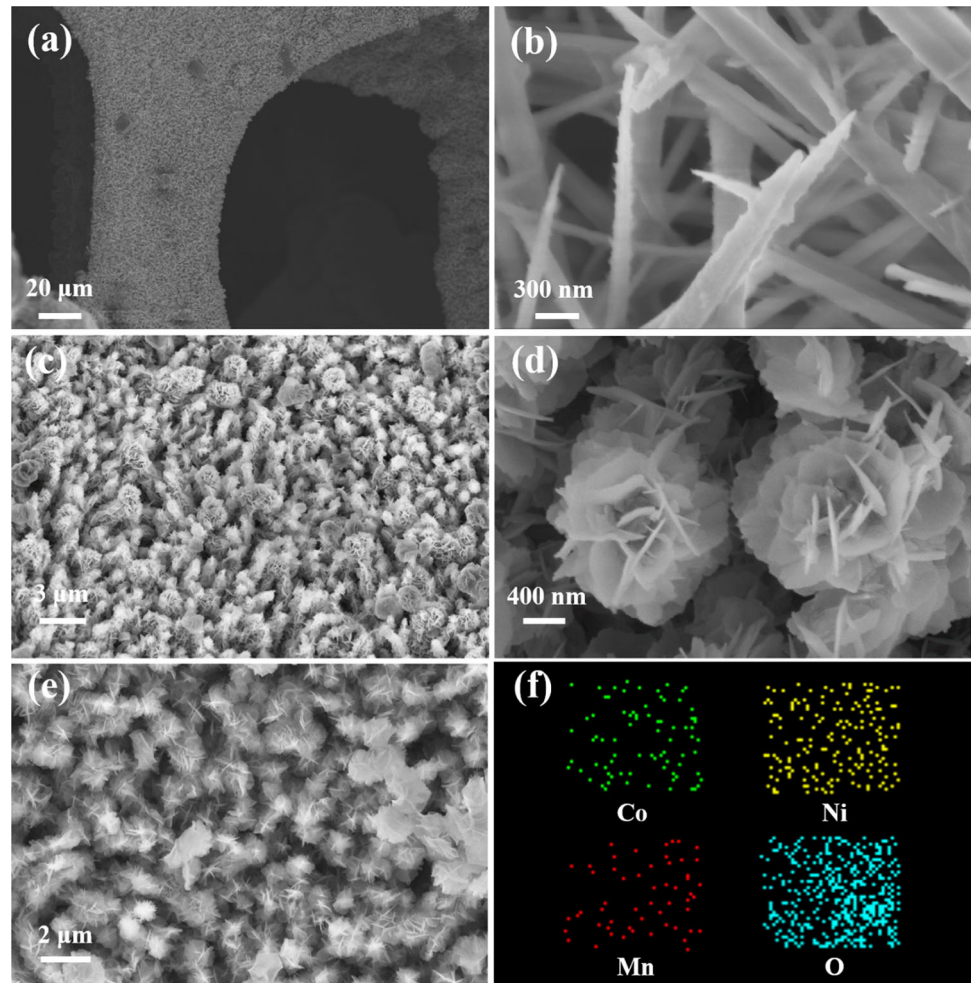


Figure 3 a XPS survey spectra of MnCo₂O₄@NiO composites. XPS survey of b Ni 2p. c Co 2p. d Mn 2p.

Figure 4 (a, b) SEM pictures of needle-like MnCo_2O_4 on the NF at various magnifications. (c, d) SEM pictures of $\text{MnCo}_2\text{O}_4@/\text{NiO}/\text{NF}$ at different magnifications. (e, f) $\text{MnCo}_2\text{O}_4@/\text{NiO}/\text{NF}$ and the corresponding EDS mapping.



hydrothermal process. And it is clear that the spherical MnCo_2O_4 presents actually a sea urchin structure formed by the polymerization of a large number of needle-like MnCo_2O_4 (displayed in Fig. S1 (a,b) of Supporting Information). The low magnification SEM picture of $\text{MnCo}_2\text{O}_4@/\text{NiO}/\text{NF}$ is presented as Fig. 4c. The $\text{MnCo}_2\text{O}_4@/\text{NiO}/\text{NF}$ with hierarchical structure is independent of each other, and there is no obvious collapse and agglomeration. In Fig. 4d, high magnification SEM image of $\text{MnCo}_2\text{O}_4@/\text{NiO}/\text{NF}$ suggests that the NiO flakes grow uniformly and densely on the surface of MnCo_2O_4 skeleton and completely envelop the needle-like MnCo_2O_4 . Moreover, the NiO flakes are interconnected with each other to form a continuous open network. After the growth of NiO, the diameter of the whole $\text{MnCo}_2\text{O}_4@/\text{NiO}/\text{NF}$ hierarchical structure becomes about $1.2\ \mu\text{m}$. For the powder deposited at the bottom of the reactor, NiO aggregates into balls of different sizes during the second hydrothermal process. Furthermore, the ball consists

of many NiO flakes agglomerated into a hydrangea shape (shown in Fig. S1 (c,d) of Supporting Information). To further confirm our samples, we selected part of the $\text{MnCo}_2\text{O}_4@/\text{NiO}/\text{NF}$ for energy dispersive spectrometer (EDS). The selected region and EDS results are shown in Fig. 4e, f, respectively. The EDS demonstrates that Co, Mn, Ni and O elements are present in the prepared core-shell structure. These elements uniformly cover the entire selected area, and the proportion of oxygen atoms is significantly higher than that of other elements, which is consistent with a higher proportion of oxygen in the $\text{MnCo}_2\text{O}_4@/\text{NiO}/\text{NF}$. The SEM images show that the synthesized material has a hierarchical structure.

The detailed structure characteristics of the samples were further identified by TEM. The darker central region and the lighter peripheral region can be clearly distinguished in a low resolution TEM (Fig. 5a). The darker central region has a pronounced needle-like boundary, which is corresponding to the

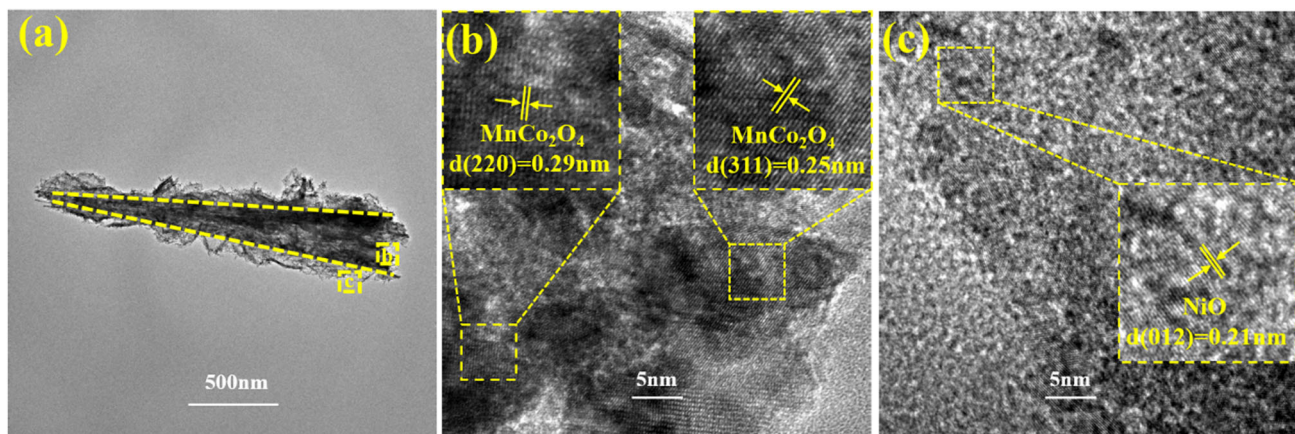
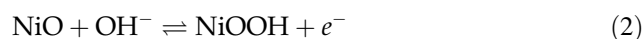
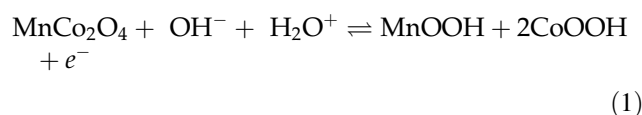


Figure 5 **a** Low resolution TEM picture of $\text{MnCo}_2\text{O}_4@\text{NiO}$. **b** High resolution TEM picture of MnCo_2O_4 in (a). **c** High resolution TEM picture of NiO in (a).

needle-like MnCo_2O_4 . On the contrary, the boundaries of the lighter peripheral region are irregular, which can be understood as the overlapping result of NiO flakes in the lateral perspective. The high resolution TEM of the region marked by b and c in Fig. 5a is clearly displayed in Fig. 5b, c. Figure 5b shows crystalline interplanar distance of 0.29 nm and 0.25 nm, which is related to the (220) and (311) crystalline interplanar distance of MnCo_2O_4 , respectively, and confirmed further by the selected area electron diffraction (SAED) pattern (Fig. S2 (b) of Supporting Information). Figure 5c presents the crystalline interplanar distance of 0.21 nm, which is corresponding to the (012) crystalline interplanar distance of NiO. The NiO nanoflakes display the polycrystalline structure, as proved by the related SAED pattern (Fig. S2 (c) of Supporting Information). The structural characteristics obtained by TEM well confirm the XRD results.

The electrochemical performance of the prepared materials was evaluated by the three-electrode setup with 2 M KOH aqueous solution as the electrolyte, Pt foil as the counter electrode and Hg/HgO electrode as the reference electrode. Figure 6a is the CV plots acquired by testing the $\text{MnCo}_2\text{O}_4@\text{NiO}/\text{NF}$ electrode under the scan rate of 2–100 mV s^{-1} . On the basis of CV plots, there are a couple of evident redox peaks, and the CV plot deviates from the rectangle, which reveals the capacitance is primarily caused by the Faraday reaction [36]. At the lower scan rates, the upward and downward peaks were related to the oxidation and reduction processes, respectively, which is connected with the following faradaic redox equations [37, 38]:



As the scan rate increases, the response current and the integral area of CV plot improve gradually because of the rapid conduction of ions and electrons, which implies the ideal capacitive behavior and good rate capability [39]. Furthermore, the oxidation peak shift toward the positive side, and reduction peak shift toward the negative side because of the increasing internal diffusion resistance in the pseudocapacitance material with the improving scan rate [40]. Figure 6b displays the GCD plots under different current densities. The tendency is similar to a regular triangle except for the platform that corresponding to the redox reaction. The discharging time becomes shorter and shorter with the increasing of current density. On the basis of formula:

$$C = \frac{I \cdot \Delta t}{m \cdot \Delta V} \quad (3)$$

The specific capacitance under various current densities could be computed. Where, I (A), t (s), m (g) and V (V) are the magnitude of current in the galvanostatic charging-discharging process, the mass of the active substance, the discharging time and the potential window in the charging and discharging process, respectively. The $\text{MnCo}_2\text{O}_4@\text{NiO}/\text{NF}$ electrode displays high specific capacitance of 1186, 1112, 1062, 970, 912 and 880 F g^{-1} under 1, 2, 3, 5, 8 and 10 A g^{-1} , respectively. We compared the CV plots of

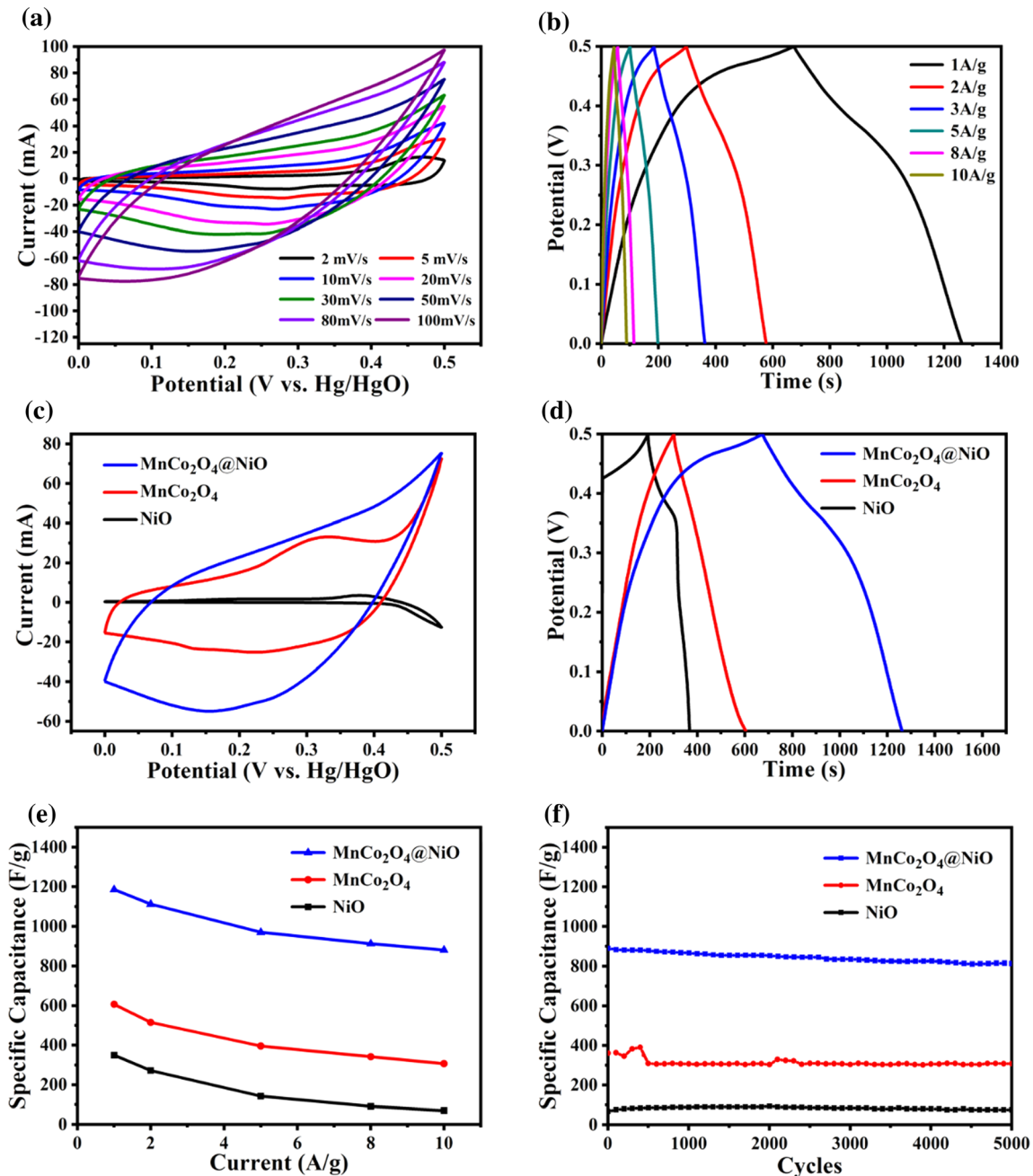


Figure 6 a CV plots of $\text{MnCo}_2\text{O}_4@\text{NiO}/\text{NF}$ under various scan rates. b GCD plots of $\text{MnCo}_2\text{O}_4@\text{NiO}/\text{NF}$ under various current densities. c CV plots at the scan rate of 50 mV s^{-1} . d GCD plots

under the current density of 1 A g^{-1} . e Specific capacitances under various current densities. f Cycle performance of NiO/NF , $\text{MnCo}_2\text{O}_4/\text{NF}$ and $\text{MnCo}_2\text{O}_4@\text{NiO}/\text{NF}$ electrodes under 10 A g^{-1} .

$\text{MnCo}_2\text{O}_4@\text{NiO}/\text{NF}$, $\text{MnCo}_2\text{O}_4/\text{NF}$ and NiO/NF electrodes under 50 mV s^{-1} , as represented in Fig. 6c. Under the same scan rate, the integral region of the $\text{MnCo}_2\text{O}_4@\text{NiO}/\text{NF}$ composite electrode is broader than that of the individual $\text{MnCo}_2\text{O}_4/\text{NF}$ and single NiO/NF electrodes, which demonstrates that the $\text{MnCo}_2\text{O}_4@\text{NiO}/\text{NF}$ electrode has higher capacitance than $\text{MnCo}_2\text{O}_4/\text{NF}$ and NiO/NF electrodes.

under the current density of 1 A g^{-1} . e Specific capacitances under various current densities. f Cycle performance of NiO/NF , $\text{MnCo}_2\text{O}_4/\text{NF}$ and $\text{MnCo}_2\text{O}_4@\text{NiO}/\text{NF}$ electrodes under 10 A g^{-1} .

Figure 6d represents the GCD plots of $\text{MnCo}_2\text{O}_4@\text{NiO}/\text{NF}$, $\text{MnCo}_2\text{O}_4/\text{NF}$ and NiO/NF electrodes under 1 A g^{-1} . For the same current density, the $\text{MnCo}_2\text{O}_4@\text{NiO}/\text{NF}$ composite electrode presents more discharge time than the $\text{MnCo}_2\text{O}_4/\text{NF}$ and NiO/NF electrodes. By the calculation, the specific capacitance of $\text{MnCo}_2\text{O}_4@\text{NiO}/\text{NF}$ composite electrode (1186 F g^{-1}) is larger than that of $\text{MnCo}_2\text{O}_4/\text{NF}$

electrode (607 F g^{-1}) and NiO/NF electrode (350 F g^{-1}) (the detailed electrochemical performance of the $\text{MnCo}_2\text{O}_4/\text{NF}$ and NiO/NF electrodes are displayed in Fig. S3 and Table S1 of Supporting Information).

The rate capability of the three electrodes was further calculated as shown in the Fig. 6e. On one hand, it is clearly seen that the specific capacitance of $\text{MnCo}_2\text{O}_4@\text{NiO}/\text{NF}$ electrode is higher than that of the $\text{MnCo}_2\text{O}_4/\text{NF}$ and NiO/NF electrodes under the current density ranges from 1 to 10 A g^{-1} . On the other hand, the composite electrode displays excellent rate capability over a single material. While the current density augments from 1 A g^{-1} to 10 A g^{-1} , the capacitance retention ratio of the $\text{MnCo}_2\text{O}_4@\text{NiO}/\text{NF}$ electrode is 74%, which is better than that of $\text{MnCo}_2\text{O}_4/\text{NF}$ electrode (50%) and NiO/NF electrode (20%). The cycle ability of the electrode is a key standard to determine whether the electrode performance is reliable. Therefore, $\text{MnCo}_2\text{O}_4@\text{NiO}/\text{NF}$, $\text{MnCo}_2\text{O}_4/\text{NF}$ and NiO/NF electrode materials were measured over 5000 cycles under 10 A g^{-1} , as displayed in Fig. 6f. The cycle curve of NiO/NF electrode is kept flat during the whole cycle and shows good cycling stability. However, its specific capacity is only about 70 F g^{-1} . It can be found from the cycle plot of the $\text{MnCo}_2\text{O}_4/\text{NF}$ electrode that the capacitance value of the electrode augments in the initial 500 cycles, which is due to the activating process of the electrode material at the beginning of the cycle test. In the subsequent cycles, the capacitance value of the electrode remains basically stable. After 5000 cycles, the specific capacity decreased to 308 F g^{-1} , which is approximately 85% of the original specific capacitance. For the cycle plot of $\text{MnCo}_2\text{O}_4@\text{NiO}/\text{NF}$ electrode, its specific capacitance value remains approximately 91% of the original capacitance value over 5000 cycles, which proves that the $\text{MnCo}_2\text{O}_4@\text{NiO}/\text{NF}$ electrode has better cyclic stability than the $\text{MnCo}_2\text{O}_4/\text{NF}$ electrode. Therefore, compared with $\text{MnCo}_2\text{O}_4/\text{NF}$ and NiO/NF electrodes, the $\text{MnCo}_2\text{O}_4@\text{NiO}$ electrode has significantly improved electrochemical performance. In addition, the $\text{MnCo}_2\text{O}_4@\text{NiO}/\text{NF}$ electrode exhibited superior specific capacitance, compared with most of MnCo_2O_4 - and NiO-based supercapacitor electrode materials reported previously (as illustrated in Table S2 of Supporting Information) such as $\text{MnCo}_2\text{O}_4@\text{NiO}$ porous nanosheets (604.5 F g^{-1} under 0.5 A g^{-1}) [27], MnCo_2O_4 nanorods and microcubes (408.33 F g^{-1}

under 5 A g^{-1}) [41], MnCo_2O_4 nanorods (845.6 F g^{-1} under 1 A g^{-1}) [42], $\text{MnCo}_2\text{O}_4@\text{N-CNF}$ meso-microporous structure (871.5 F g^{-1} under 0.5 A g^{-1}) [43], $\text{MnCo}_2\text{O}_4@\text{MnO}_2$ (858 F g^{-1} under 1 A g^{-1}) [44] and $\text{CNT}@\text{NiO}$ (996 F g^{-1} under 1 A g^{-1}) [45].

For further analysis of the electrochemical behaviors of the electrodes, electrochemical impedance spectroscopy (EIS) of the three samples was detected under the frequency interval of 0.01–100 kHz and 5 mV amplitude, as displayed in Fig. 7. At low frequencies, an approximately vertical line indicates the typical capacitive behavior. In the higher frequency zone, the intercept of the real axis and semicircular radius of Nyquist plots are connected with the series resistance (R_s) and charge-transferring resistance (R_{ct}), respectively [46]. Further, the simulation of Z-view software is used to quantitatively fit the equivalent resistance R_s and R_{ct} . The equivalent circuit is shown in the illustration, in which the Z_w and C_{dl} correspond to Warburg impedance and the double layer capacitance, respectively. The R_s of $\text{MnCo}_2\text{O}_4@\text{NiO}/\text{NF}$, $\text{MnCo}_2\text{O}_4/\text{NF}$ and NiO/NF electrodes was fitted to be 0.15Ω , 0.21Ω and 0.94Ω , respectively. Meanwhile, the R_{ct} of $\text{MnCo}_2\text{O}_4@\text{NiO}/\text{NF}$, $\text{MnCo}_2\text{O}_4/\text{NF}$ and NiO/NF electrodes was determined to be 1.20Ω , 2.21Ω and 7.20Ω , respectively. The $\text{MnCo}_2\text{O}_4@\text{NiO}/\text{NF}$ electrode exhibits lower series resistance and charge-transfer resistance than $\text{MnCo}_2\text{O}_4/\text{NF}$ and NiO/NF electrodes. The lower resistance is due to that the better designed hierarchical structure with needle-like MnCo_2O_4 and NiO flakes effectively shortened the distance of ion diffusion path [29]. Consequently, the diffusion and

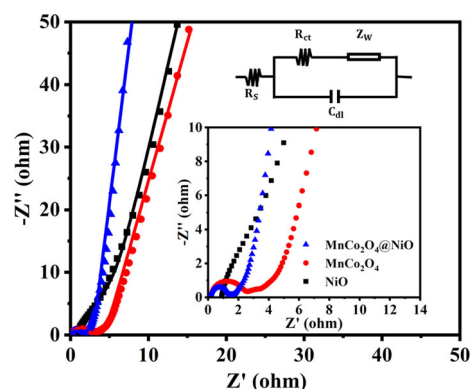


Figure 7 Nyquist curves of NiO/NF, $\text{MnCo}_2\text{O}_4/\text{NF}$ and $\text{MnCo}_2\text{O}_4@\text{NiO}/\text{NF}$ electrodes. The illustrations display the middle and high frequency region of Nyquist curves and equivalent circuit model, respectively.

migration of ions and electrons are greatly promoted during the fast charging-discharging process, which helps to understand the better electrochemical properties of $\text{MnCo}_2\text{O}_4@\text{NiO}/\text{NF}$ electrode than $\text{MnCo}_2\text{O}_4/\text{NF}$ and NiO/NF electrodes. After 5000 cycles, as shown in Fig. S4 of Supporting Information, the R_s and R_{ct} of $\text{MnCo}_2\text{O}_4@\text{NiO}/\text{NF}$ electrode increase a little to 0.17Ω and 1.67Ω , respectively, which further demonstrates a small resistance change and superior cyclic stability.

From another point of view, we also fitted the peak current of the sample under various sweep rates with the square root of the sweep rate, as displayed in Fig. 8. The three straight lines in fitting results show that the redox reaction in the electrode material is the diffusion-dominated process. The diffusion coefficient of OH^- in the three electrochemical processes can be calculated by Randles–Sevcik equation. The equation is described as follows [47]:

$$i_p = 2.69 \times 10^5 \times n^{\frac{3}{2}} \times A \times v^{\frac{1}{2}} \times D^{\frac{1}{2}} \times C \quad (4)$$

where i_p (A), A (cm^2), v (V/s), D ($\text{cm}^2 \text{s}^{-1}$) and C are the peak current, the area electrode, the sweep rate, the diffusion coefficient and the concentration of OH^- in the solution, respectively. n is the number of electrons transferred in the electrochemical process, which could be determined by the two equations mentioned above (Eq. (1) and (2)). The ratio of diffusion coefficient between $\text{MnCo}_2\text{O}_4@\text{NiO}$ and MnCo_2O_4 is calculated as:

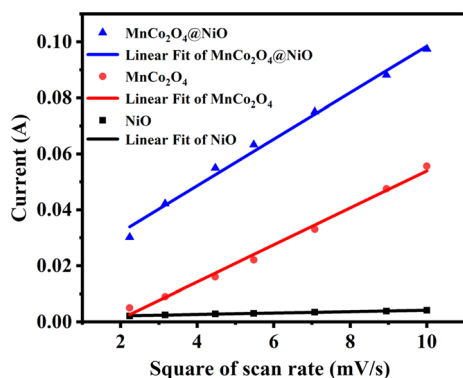


Figure 8 Linear relationships on the cathode peak current and the square root of the sweep rate for the three electrodes.

$$\begin{aligned} & D(\text{MnCo}_2\text{O}_4@\text{NiO})/D(\text{MnCo}_2\text{O}_4) \\ &= \left[\left(\frac{i_p}{\sqrt{v}} \right) \left(\text{NiO}@\text{MnCo}_2\text{O}_4 \right) / \left(\frac{i_p}{\sqrt{v}} \right) \right. \\ & \quad \left. (\text{MnCo}_2\text{O}_4) \right]^2 = 1.58 \end{aligned} \quad (5)$$

The results show that OH^- has a high diffusion coefficient in the $\text{MnCo}_2\text{O}_4@\text{NiO}$ composite electrode. In particular, NiO exhibits the lowest diffusion coefficient due to the coating process. The results of diffusion coefficient analysis are consistent with the impedance analysis that the $\text{MnCo}_2\text{O}_4@\text{NiO}/\text{NF}$ electrode exhibits lower charge-transfer resistance. The $\text{MnCo}_2\text{O}_4@\text{NiO}/\text{NF}$ electrode has a higher diffusion coefficient, suggesting that there is weaker ion transport obstruction during the reaction. All of these are contributed to a better understanding of the superior electrochemical performance of $\text{MnCo}_2\text{O}_4@\text{NiO}/\text{NF}$ composite electrode.

For the sake of exploring the potential application of $\text{MnCo}_2\text{O}_4@\text{NiO}$ electrode materials in supercapacitor devices, ASC device based on $\text{MnCo}_2\text{O}_4@\text{NiO}/\text{NF}$ electrode and AC/NF electrode is assembled as displayed in the Fig. 9a. In this ASC device, fiberglass filter paper and 2 M KOH are used for the membrane and electrolyte, respectively. Subsequent measurements of the electrochemical properties of the ASC devices are based on this configuration. It is necessary to confirm the proper working potential range for studying the properties of the device. Figure 9b exhibited the CV plots under 5 mV s^{-1} of AC/NF electrode in the potential window of -1 V – 0 V and $\text{MnCo}_2\text{O}_4@\text{NiO}/\text{NF}$ electrode in the voltage window of 0 V – 0.5 V . The CV plots imply that two-electrode materials work stably within their test voltage range. Based on this result, the stable operating potential range of the ASC device could be expanded to the aggregation of the positive and negative electrode voltage ranges (1.5 V).

The CV plots of ASC device under various scan rates were represented as Fig. 9c. The profile of CV plots gradually deviates from the rectangle along with scan rate augmenting. Besides, the peak current augments with scan rate. For the GCD test of the ASC device under various current densities, the applied current is computed by multiplying the sum of the two-electrode active mass with the related current density. Figure 9d, e display the GCD plots and the related specific capacitances under various current densities. The specific capacitances for the ASC

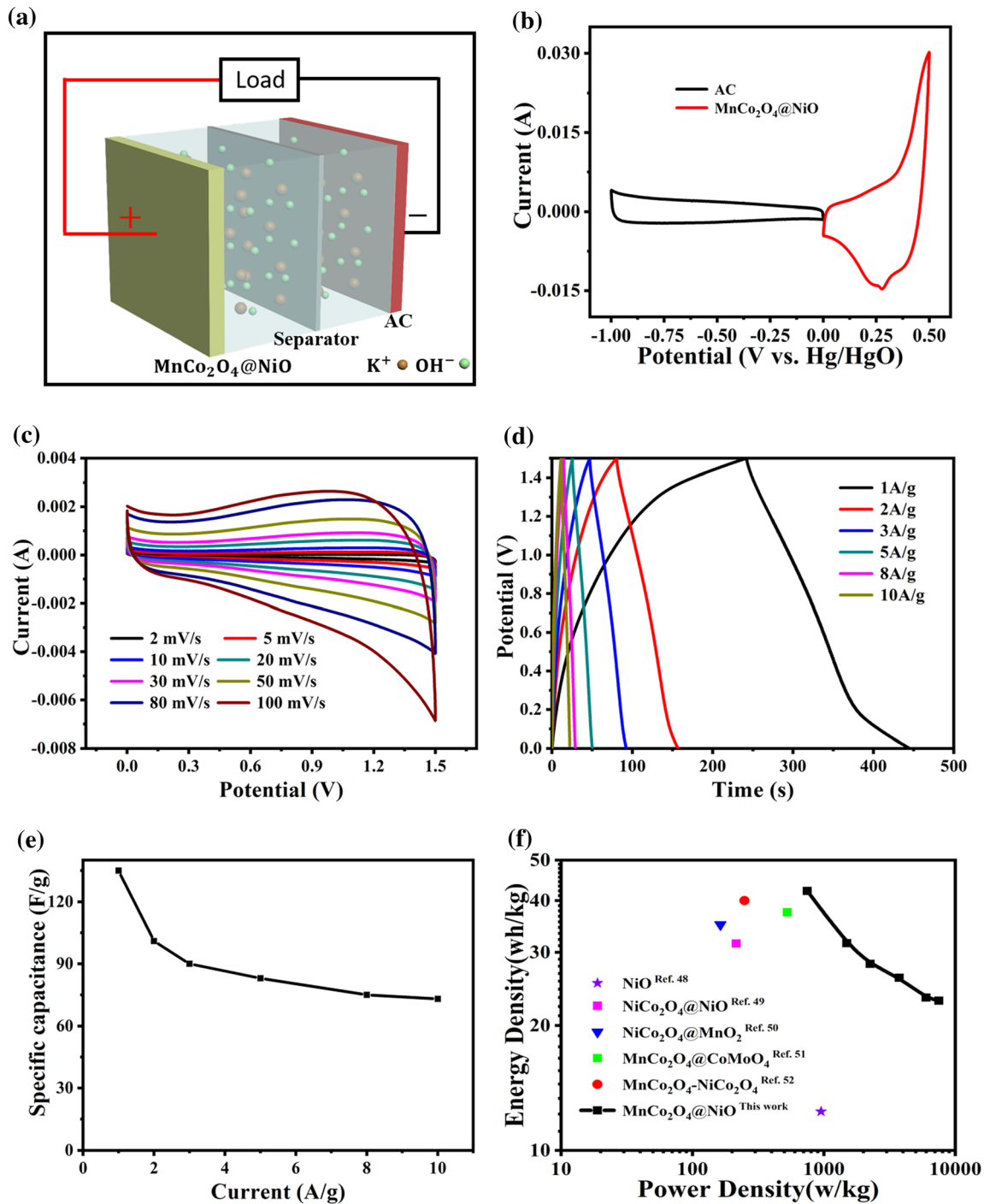


Figure 9 a Assembly structure diagram of MnCo₂O₄@NiO/NF-based ASC device. b CV measurements for the positive and negative electrodes under 5 mV s⁻¹. c CV plots of the ASC device under various scan rates. d GCD plots under various current

device at 1 A g⁻¹, 2 A g⁻¹, 3 A g⁻¹, 5 A g⁻¹, 8 A g⁻¹ and 10 A g⁻¹ are 135 F g⁻¹, 101 F g⁻¹, 90 F g⁻¹, 83 F g⁻¹, 74 F g⁻¹ and 73 F g⁻¹, respectively. In order to better estimate the energy storage ability of the ASC,

densities. e The specific capacitance under various current densities. f Ragone plot of energy density and power density for the as-prepared ASC devices.

the relationship on energy density and power density was drawn in Fig. 9f. The energy density and power density could be calculated as follows [6]:

$$E = C \cdot \Delta V^2 / 2 \quad (6)$$

$$P = E / \Delta t \quad (7)$$

where C is specific capacitance, ΔV is voltage window, and Δt is discharging time. The computed results are summarized in the Fig. 9f. A energy density of the ASC is computed to be 42.2 Wh kg^{-1} under 748.2 W kg^{-1} . Further, while the power density augments to 7499.7 W kg^{-1} , the ASC device remains the energy density of 22.9 Wh kg^{-1} . The energy storage ability of $\text{MnCo}_2\text{O}_4@/\text{NiO}/\text{NF}$ -based ASC device is better than that of most of manganese and nickel oxides-based ASC devices reported previously, such as NiO (12.4 Wh kg^{-1} under 985 W kg^{-1}) [48], $\text{NiCo}_2\text{O}_4@/\text{NiO}$ (31.5 Wh kg^{-1} under 215.2 W kg^{-1}) [49], $\text{NiCo}_2\text{O}_4@/\text{MnO}_2$ (35 Wh kg^{-1} under 163 W kg^{-1}) [50], $\text{MnCo}_2\text{O}_4@/\text{CoMoO}_4$ (37.5 Wh kg^{-1} under 527.8 W kg^{-1}) [51] and $\text{MnCo}_2\text{O}_4@/\text{NiCo}_2\text{O}_4$ (40 Wh kg^{-1} under 248.7 W kg^{-1}) [52]. Furthermore, the capacitance retention of the $\text{MnCo}_2\text{O}_4@/\text{NiO}/\text{NF}$ -based ASC device has an acceptable deterioration with conservation of 79.4% over 5000 cycles under 5 A g^{-1} , which reveals the ASC device has a good stability (displayed in Fig. S5 of Supporting Information). The related Coulombic efficiency of the ASC device is over 94.4% during the 5000 cycles (Fig. S6 of Supporting Information), showing the highly reversible electrochemical reactions.

Conclusion

The $\text{NiO}@/\text{MnCo}_2\text{O}_4$ hierarchical structures were directly deposited on NF as the additive-free supercapacitor electrode with simple hydrothermal method and annealing processes. The $\text{MnCo}_2\text{O}_4@/\text{NiO}/\text{NF}$ electrode presented higher specific capacitance (1186 F g^{-1}) than MnCo_2O_4 (607 F g^{-1}) and NiO (350 F g^{-1}) electrodes under 1 A g^{-1} . The $\text{MnCo}_2\text{O}_4@/\text{NiO}/\text{NF}$ electrode also exhibited excellent cycling performance (remaining 91% of the original capacitance over 5000 cycles under 10 A g^{-1}) and super rate capability. Based on the analysis of EIS and diffusion coefficient, we find that the construction of hierarchical structure in the $\text{MnCo}_2\text{O}_4@/\text{NiO}/\text{NF}$ electrode not only greatly promotes the diffusion and migration of ions and electrons in rapid reaction, but also greatly reduces the volume deformation and

structure collapsing of the electrode materials during the charge–discharge processes, thus achieving improved electrochemical performance. In addition, an ASC device with high energy density was assembled with the $\text{MnCo}_2\text{O}_4@/\text{NiO}/\text{NF}$ and AC/NF as the positive and negative electrodes, respectively. The assembled ASC manifested higher energy density of 42.2 Wh kg^{-1} under 748.2 W kg^{-1} and still hold the energy density of 22.9 Wh kg^{-1} while the power density increased tenfold to 7499.7 W kg^{-1} . Especially, the ASC device preserved 79.4% specific capability over 5000 cycles. Therefore, the $\text{MnCo}_2\text{O}_4@/\text{NiO}/\text{NF}$ with hierarchical structure is proved to be the promising material for enhanced performance energy storage device.

Acknowledgements

The work is financially supported by the National Natural Science Foundation of China (Grant No. 51572218), and the Key Project of Research & Development of Shaanxi Province in China (No. 2018ZDCXL-GY-08-05).

Compliance with ethical standards

Conflict of interest The authors declare that there is no conflict of interest regarding the publication of this article.

Supplementary Information: The online version of this article (<https://doi.org/10.1007/s10853-021-05810-8>) contains supplementary material, which is available to authorized users.

References

- [1] Simon P, Gogotsi Y (2008) Materials for electrochemical capacitors. *Nat Mater* 7(11):845–854
- [2] Wang G, Zhang L, Zhang J (2012) A review of electrode materials for electrochemical supercapacitors. *Chem Soc Rev* 41(2):797–828
- [3] Zhang LL, Zhao XS (2009) Carbon-based materials as supercapacitor electrodes. *Chem Soc Rev* 38(9):2520–2531
- [4] Kötz R, Carlen M (2000) Principles and applications of electrochemical capacitors. *Electrochim Acta* 45(15–16):2483–2498

- [5] Liu C, Yu Z, Neff D, Zhamu A, Jang BZ (2010) Graphene-based supercapacitor with an ultrahigh energy density. *Nano Lett* 10(12):4863–4868
- [6] Fan Z, Yan J, Wei T, Zhi L, Ning G, Li T, Wei F (2011) Asymmetric supercapacitors based on graphene/mno₂ and activated carbon nanofiber electrodes with high power and energy density. *Adv Funct Mater* 21(12):2366–2375
- [7] Béguin F, Presser V, Balducci A, Frackowiak E (2014) Carbons and electrolytes for advanced supercapacitors. *Adv Mater* 26(14):2219–2251
- [8] Yu G, Hu L, Liu N, Wang H, Vosgueritchian M, Yang Y, Cui Y, Bao Z (2011) Enhancing the Supercapacitor Performance of Graphene/MnO₂ Nanostructured Electrodes by Conductive Wrapping. *Nano Lett* 11(10):4438–4442
- [9] Zhi M, Xiang C, Li J, Li M, Wu N (2013) Nanostructured carbon-metal oxide composite electrodes for supercapacitors: a review. *Nanoscale* 5(1):72–88
- [10] Zhang Y, Li L, Su H, Huang W, Dong X (2015) Binary metal oxide: advanced energy storage materials in supercapacitors. *J Mater Chem A* 3(1):43–59
- [11] Pasero D, Reeves N, West A (2005) Co-doped MnO: a possible anode material for lithium batteries. *J Power Sources* 141(1):156–158
- [12] Hui KN, Hui KS, Tang Z, Jadhav VV, Xia QX (2016) Hierarchical chestnut-like MnCo₂O₄ nanoneedles grown on nickel foam as binder-free electrode for high energy density asymmetric supercapacitors. *J Power Sources* 330:195–203
- [13] Song D, Zhu J, Li J, Pu T, Huang B, Zhao C, Xie L, Chen L (2017) Free-standing two-dimensional mesoporous ZnCo₂O₄ thin sheets consisting of 3D ultrathin nanoflake array frameworks for high performance asymmetric supercapacitor. *Electrochim Acta* 257:455–464
- [14] Vigneshwaran P, Kandiban M, Senthil Kumar N, Venkatchalam V, Jayavel R, Vetha Potheher I (2016) A study on the synthesis and characterization of CoMn₂O₄ electrode material for supercapacitor applications. *J Mater Sci-Mater Electron* 27(5):4653–4658
- [15] Zeng J, Ren Y, Wang S, Hao Y, Wu H, Zhang S, Xing Y (2017) Hierarchical porous ZnMn₂O₄ microspheres assembled by nanosheets for high performance anodes of lithium ion batteries. *Inorg Chem Front* 4(10):1730–1736
- [16] Vadiyar MM, Kolekar SS, Deshpande NG, Chang J-Y, Kashale AA, Ghule AV (2016) Binder-free chemical synthesis of ZnFe₂O₄ thin films for asymmetric supercapacitor with improved performance. *Ionics* 23(3):741–749
- [17] Lv J, Liang T, Yang M, Ken S, Hideo M (2017) Performance comparison of NiCo₂O₄ and NiCo₂S₄ formed on Ni foam for supercapacitor. *Compos Pt B-Eng* 123:28–33
- [18] Lv J, Guo W, Liang T (2016) Synthesis of Co₃O₄@CoMoO₄ core-shell architectures nanocomposites as high-performance supercapacitor electrode. *J Electroanal Chem* 783:250–257
- [19] Li L, Zhang Y, Shi F, Zhang Y, Zhang J, Gu C, Wang X, Tu J (2014) Spinel manganese-nickel-cobalt ternary oxide nanowire array for high-performance electrochemical capacitor applications. *ACS Appl Mater Interfaces* 6(20):18040–18047
- [20] Mondal AK, Su D, Chen S, Ung A, Kim H-S, Wang G (2015) Mesoporous MnCo₂O₄ with a flake-like structure as advanced electrode materials for lithium-ion batteries and supercapacitors. *Chem-Eur J* 21(4):1526–1532
- [21] Liu S, Hui KS, Hui KN (2015) 1 D hierarchical MnCo₂O₄ nanowire@MnO₂ sheet core-shell arrays on graphite paper as superior electrodes for asymmetric supercapacitors. *Chem Nano Mat* 1(8):593–602
- [22] Liu S, Hui KS, Hui KN, Yun JM, Kim KH (2016) Vertically Stacked bilayer CuCo₂O₄/MnCo₂O₄ heterostructures on functionalized graphite paper for high-performance electrochemical capacitors. *J Mater Chem A* 4(21):8061–8071
- [23] Liu S, Ni D, Li HF, Jun SC, Hui KN, Ouyang CY (2018) Effect of cation substitution on pseudocapacitive performance of spinel cobaltite MCo₂O₄ (M = Mn, Ni, Cu, and Co). *J Mater Chem A* 6(23):10674–10685
- [24] Zhao Y, Hu L, Zhao S, Wu L (2016) Preparation of MnCo₂O₄@Ni(OH)₂ core-shell flowers for asymmetric supercapacitor materials with ultrahigh specific capacitance. *Adv Funct Mater* 26(23):4085–4093
- [25] Kim S-I, Lee J-S, Ahn H-J, Song H-K, Jang J-H (2013) Facile route to an efficient NiO supercapacitor with a three-dimensional nanonetwork morphology. *ACS Appl Mater Interfaces* 5(5):1596–1603
- [26] Li T, Li X, Wang Z, Guo H, Hu Q, Peng W (2016) Robust synthesis of hierarchical mesoporous hybrid NiO-MnCo₂O₄ microspheres and their application in Lithium-ion batteries. *Electrochim Acta* 191:392–400
- [27] Cheng B, Zhang W, Yang M, Zhang Y, Meng F (2019) Preparation and study of porous MnCo₂O₄@NiO nanosheets for high-performance supercapacitor. *Ceram Int* 45(16):20451–20457
- [28] Jiang L, Yuan X, Liang J, Zhang J, Wang H, Zeng G (2016) Nanostructured core-shell electrode materials for electrochemical capacitors. *J Power Sources* 331:408–425
- [29.] Ho K-C, Lin L-Y (2019) A review of electrode materials based on core-shell nanostructures for electrochemical supercapacitors. *J Mater Chem A* 7(8):3516–3530
- [30] Shinde NM, Yun JM, Mane RS, Mathur S, Kim KH (2018) An Overview of Self-Grown Nanostructured Electrode Materials in Electrochemical Supercapacitors. *J Korean Ceram Soc* 55(5):407–418

- [31] Cheng J, Zhao B, Zhang W, Shi F, Zheng G, Zhang D, Yang J (2015) High-performance supercapacitor applications of NiO-nanoparticle-decorated millimeter-long vertically aligned carbon nanotube arrays via an effective supercritical CO₂-assisted method. *Adv Funct Mater* 25(47):7381–7391
- [32] Sahoo S, Shim J-J (2016) Facile synthesis of three-dimensional ternary ZnCo₂O₄/reduced graphene oxide/NiO composite film on nickel foam for next generation supercapacitor electrodes. *ACS Sustain Chem Eng* 5(1):241–251
- [33] Wu Z, Ren W, Wen L, Gao L, Zhao J, Chen Z, Zhou G, Li F, Cheng H (2010) Graphene anchored with Co₃O₄ nanoparticles as anode of lithium ion batteries with enhanced reversible capacity and cyclic performance. *ACS Nano* 6(4):3187–3194
- [34] Chuang TJ, Brundle CR, Rice DW (1976) Interpretation of the x-ray photoemission spectra of cobalt oxides and cobalt oxide surfaces. *Surf Sci* 59(2):413–429
- [35] Li L, He F, Gai S, Zhang S, Gao P, Zhang M, Chen Y, Yang P (2014) Hollow structured and flower-like C@MnCo₂O₄ composite for high electrochemical performance in a supercapacitor. *Cryst Eng Comm* 16(42):9873–9881
- [36] Wu Z-S, Wang D-W, Ren W, Zhao J, Zhou G, Li F, Cheng H-M (2010) Anchoring hydrous RuO₂ on graphene sheets for high-performance electrochemical capacitors. *Adv Funct Mater* 20(20):3595–3602
- [37] Tholkappian R, Naveen AN, Sumithra S, Vishista K (2015) Investigation on spinel MnCo₂O₄ electrode material prepared via controlled and uncontrolled synthesis route for supercapacitor application. *J Mater Sci* 50(17):5833–5843
- [38] Yuan C, Zhang X, Su L, Gao B, Shen L (2009) Facile synthesis and self-assembly of hierarchical porous NiO nano/micro spherical superstructures for high performance supercapacitors. *J Mater Chem* 19(32):5772–5777
- [39] Lu X, Zhai T, Zhang X, Shen Y, Yuan L, Hu B, Gong L, Chen J, Gao Y, Zhou J, Tong Y, Wang ZL (2012) WO₃·x@Au@MnO₂ core-shell nanowires on carbon fabric for high-performance flexible supercapacitors. *Adv Mater* 24(7):938–944
- [40] Ji J, Zhang LL, Ji H, Li Y, Ruoff RS (2013) Nanoporous Ni(OH)₂ thin film on 3D ultrathin-graphite foam for asymmetric supercapacitor. *ACS Nano* 7(7):6237–6243
- [41] Shi X, Liu Z, Zheng Y, Zhou G (2017) Controllable synthesis and electrochemical properties of MnCo₂O₄ nanorods and microcubes. *Coll Surf A-Physicochem Eng Asp* 522:525–535
- [42] Xu J, Sun Y, Lu M, Wang L, Zhang J, Tao E, Qian J, Liu X (2018) Fabrication of the porous MnCo₂O₄ nanorod arrays on Ni foam as an advanced electrode for asymmetric supercapacitors. *Acta Mater* 152:162–174
- [43] Cai N, Fu J, Chan V, Liu M, Chen W, Wang J, Zeng H, Yu F (2019) MnCo₂O₄@nitrogen-doped carbon nanofiber composites with meso-microporous structure for high-performance symmetric supercapacitors. *J Alloy Compd* 782:251–262
- [44] Zheng X, Ye Y, Yang Q, Geng B, Zhang X (2016) Hierarchical structures composed of MnCo₂O₄@MnO₂ core-shell nanowire arrays with enhanced supercapacitor properties. *Dalton Trans* 45(2):572–578
- [45] Yi H, Wang H, Jing Y, Peng T, Wang X (2015) Asymmetric supercapacitors based on carbon nanotubes@NiO ultrathin nanosheets core-shell composites and MOF-derived porous carbon polyhedrons with super-long cycle life. *J Power Sources* 285:281–290
- [46] Zhao P, Li W, Wang G, Yu B, Li X, Bai J, Ren Z (2014) Facile hydrothermal fabrication of nitrogen-doped graphene/Fe₂O₃ composites as high performance electrode materials for supercapacitor. *J Alloy Compd* 604:87–93
- [47] Ren X, Zhao Q, McCulloch WD, Wu Y (2017) MoS₂ as a long-life host material for potassium ion intercalation. *Nano Res* 10(4):1313–1321
- [48] Zhang S, Yin B, Wang Z, Peter F (2016) Super long-life all solid-state asymmetric supercapacitor based on NiO nanosheets and α-Fe₂O₃ nanorods. *Chem Eng J* 306:193–203
- [49] Liu X, Liu J, Sun X (2015) NiCo₂O₄@NiO hybrid arrays with improved electrochemical performance for pseudocapacitors. *J Mater Chem A* 3(26):13900–13905
- [50] Xu K, Li W, Liu Q, Li B, Liu X, An L, Chen Z, Zou R, Hu J (2014) Hierarchical mesoporous NiCo₂O₄@MnO₂ core-shell nanowire arrays on nickel foam for aqueous asymmetric supercapacitors. *J Mater Chem A* 2(13):4795–4802
- [51] Feng Y, Liu W, Sun L, Zhu Y, Chen Y, Meng M, Li J, Yang J, Zhang Y, Liu K (2018) Hierarchical MnCo₂O₄@CoMoO₄ core-shell nanowire arrays supported on Ni foam for supercapacitor. *J Alloy Compd* 753:761–770
- [52] Lee H-M, V. V. Muralee Gopi C, Rana PJS, Vinodh R, Kim S, Padma R, Kim H-J, (2018) Hierarchical nanostructured MnCo₂O₄-NiCo₂O₄ composites as innovative electrodes for supercapacitor applications. *New J Chem* 42(21):17190–17194

Publisher's Note Springer Nature remains neutral with regard to jurisdictional claims in published maps and institutional affiliations.